

Analysis of coherent dynamics of a Rydberg-atom quantum simulatorHikaru Tamura,^{1,*} Tomotake Yamakoshi,² and Ken'ichi Nakagawa²¹*Department of Physics, University of Michigan, Ann Arbor, Michigan 48109, USA*²*Institute for Laser Science, University of Electro-Communications, 1-5-1 Chofugaoka, Chofu, Tokyo 182-8585, Japan*

(Received 6 February 2020; accepted 1 April 2020; published 28 April 2020)

Studying dynamics is one of the most challenging areas of quantum many-body physics. In recent years, an attractive platform based on Rydberg atoms has been used to probe it since tunable interactions between Rydberg atoms enable a system to form interesting Hamiltonians. However, the observed dynamics generally differs from a desired Hamiltonian because an experimental system has various physical limitations and technical imperfections. In this work, to explain discrepancies from an ideal situation we modify the pure Hamiltonian to dissipative model including known imperfections, and the numerical model is compared with experimentally observed dynamics. As the experimental system, we use arrays with up to six atoms that are confined in one and two dimensions and coupled to nD -Rydberg states. By comparing results of the numerical simulation with observed dynamics, we analyze the contributions of individual imperfections to the obtained dynamics. Such analysis provides useful information for improving an experimental simulator and is an essential step for scaling up the number of atoms.

DOI: [10.1103/PhysRevA.101.043421](https://doi.org/10.1103/PhysRevA.101.043421)**I. INTRODUCTION**

In recent years, much attention has been paid to develop well-controlled quantum systems to study quantum many-body physics [1] and realize universal quantum computations [2]. Although various experimental platforms have been proposed and developed, an approach based on arrays of neutral atoms is a promising candidate for scaling up the number of qubits [3–5]. Their weak interactions with environment provide a well-isolated system that leads to single-qubit operations between their ground states with high fidelities [6,7]. Through developments in laser-trapping techniques [8–15], reconfigurable arrays constructed with a large number of atoms are now achieved while keeping the individual distinguishability and accessibility. Strong interactions between atoms can be created by exciting them to Rydberg states which have large dipole moments compared to ground states [16]. Since their interaction strength depends on atomic separation and selected Rydberg states, this system has a tunable interaction range. In particular, a combination with a reconfigurable array of atoms becomes a flexible platform for studying quantum many-body physics. Recent experiments based on individual Rydberg atoms [17] have probed a wide variety of quantum many-body phenomena, such as Ising-type [18–21] and XY spin models [22].

However, experimental systems include not only coherent dynamics described by the desired Hamiltonian but also physical limitations and technical imperfections. Even if individual imperfections are small, they accumulate and affect the dynamics, which results in difficulties for scaling up the number of qubits. Therefore, it is essential to understand the origins of these imperfections as well as their influence on

the dynamics. These investigations provide insights for improving the abilities of the quantum simulators.

There is progress in recent theoretical analysis for this purpose. The origins of imperfections that lead to damping and amplitude limitations of Rabi oscillations between ground and Rydberg states at the level of a single atom are studied in [23]. The numerical simulation model including individually measured physical limitations and technical imperfections explains measured single-atom Rabi oscillations. In addition, a model based on a Lindblad master equation is developed for simulating many-body dynamics [24]. The observed dynamics of up to five atoms confined in a linear or a zigzag array and excited to nS -Rydberg states are reproduced by the numerical model.

In this paper, we experimentally demonstrate quantum many-body dynamics with up to six ^{87}Rb atoms confined in various two-dimensional geometries and excited to nD -Rydberg states, where the interaction is varied from fully blockaded to blockade-breaking and nearest-neighbor blockaded regimes. The observed dynamics are compared with a numerical model that includes various physical limitations and technical imperfections arising not only from the single-atom level but also from the multiparticle level. These investigations clarify the contribution of individual imperfections to the many-body system.

This paper is organized as follows. Section II presents our experimental setup and procedure for probing many-body quantum dynamics. In addition, we introduce a pure Hamiltonian which briefly describes the system. In Sec. III, we modify the pure Hamiltonian to include physical limitations and technical imperfections in our system. Section IV shows experimentally observed dynamics in two different interaction regimes: The first is a strong interaction regime in which interaction strengths of atomic pairs are larger than driving Rabi frequencies. The second is when only neighboring pairs have

*tamurah@umich.edu

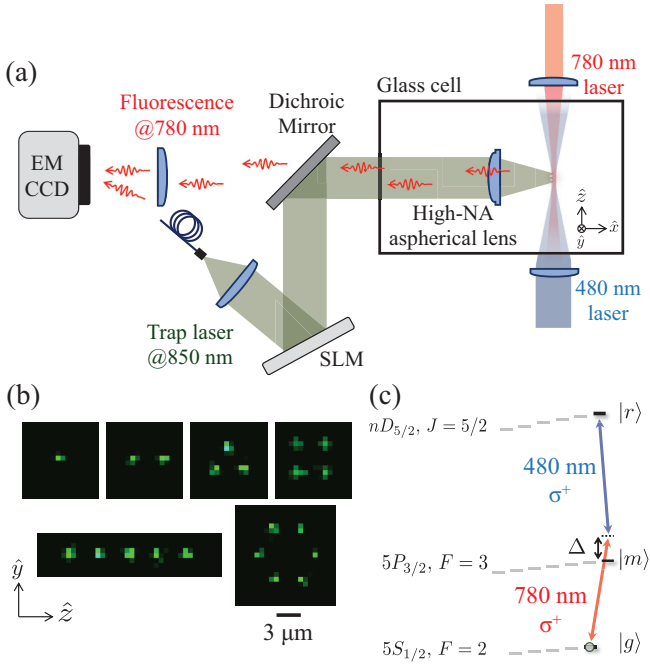


FIG. 1. (a) Schematic of the experimental setup. The trap beam at 850 nm is reflected by a spatial light modulator (SLM) and strongly focused with a numerical aperture (NA) = 0.5 aspherical lens located inside the ultrahigh vacuum glass cell. The atomic fluorescence at 780 nm is separated from the trap beam by a dichroic mirror and imaged with an EMCCD camera. (b) Single-shot fluorescence images of single-atom arrays used in this work. The arrays are aligned in the \hat{y} - \hat{z} plane and have a nearest-neighbor distance of $d \approx 3.0 \mu\text{m}$, where \hat{z} is the quantization axis. (c) Energy levels involved in the Rydberg excitation. Each atom is coherently driven by global two-photon excitation lasers, circularly polarized 780- and 480-nm lasers. Their single-photon Rabi frequencies are denoted as Ω_{780} and Ω_{480} , respectively. With the large intermediate detuning $\Delta (\gg \Omega_{780}, \Omega_{480})$, the description of the atom is reduced to a two-level model of the ground state $|g\rangle = |5S_{1/2}, F = 2, m_F = 2\rangle$ and the Rydberg state $|r\rangle = |nD_{5/2}, m_J = 5/2\rangle$ with an effective two-photon Rabi frequency $\Omega = \Omega_{780}\Omega_{480}/(2\Delta)$.

strong interactions. The observed dynamics are compared with the numerical simulation. The comparison is discussed in Sec. V. A summary is given in Sec. VI.

II. EXPERIMENTAL SETUP AND PROCEDURE

Our experimental setup is sketched in Fig. 1(a). Our experimental sequence begins with a three-dimensional magneto-optical trap (MOT) around a holographic array of optical microtraps [9]. Each trap has a beam waist of $1.0 \mu\text{m}$ and a trap depth of 1.2 mK and is stochastically loaded from the MOT with a single ^{87}Rb atom with a probability of ~ 0.5 due to the collisional blockade mechanism [25]. After a 60-ms loading phase, we remove the MOT cloud by switching off the magnetic field gradient and the MOT beams. The fluorescence of trapped atoms is induced by a near-resonant imaging beam and detected by a cooled electron-multiplying CCD (EMCCD) camera with 20-ms exposure time. When the EMCCD has finished acquiring the fluorescence, a computer

reads the image and analyzes the atomic configuration in the array. These procedures are repeated with a repetition rate of $\approx 12 \text{ Hz}$ until all microtraps are filled with a single atom. Once a fully loaded array is ready, we take an additional fluorescence image after polarization-gradient cooling, which yields an initial atomic configuration. Figure 1(b) shows the single-shot fluorescence images of various geometries of arrays used in this work.

After the initial atomic configuration is recorded, a bias magnetic field of $\approx 3.4 \text{ G}$ along the \hat{z} axis is turned on, and each trap depth is adiabatically decreased to $\approx 0.48 \text{ mK}$. Then, the atoms are optically pumped in $|g\rangle = |5S_{1/2}, F = 2, m_F = 2\rangle$. At the end of the optical pumping phase, the atoms have a temperature of $35(4) \mu\text{K}$ measured by the release and recapture method [26]. To coherently excite atoms to a Rydberg state $|r\rangle = |nD_{5/2}, m_J = 5/2\rangle$, we apply global two-photon excitation lasers, a σ^+ -polarized 780-nm laser and a σ^+ -polarized 480-nm laser. The excitation lasers provide a driving Rabi frequency $\Omega = \Omega_{780}\Omega_{480}/(2\Delta)$ between $|g\rangle$ and $|r\rangle$, where Ω_{780} and Ω_{480} are single-photon Rabi frequencies and $\Delta/(2\pi) \approx 740 \text{ MHz}$ is a detuning from an intermediate state $|m\rangle = |5P_{3/2}, F = 3, m_F = 3\rangle$ [Fig. 1(c)]. The values of $(\Omega_{780}, \Omega_{480})/(2\pi)$ averaged over all experiments are $\approx (80, 25) \text{ MHz}$. The excitation lasers are turned on for duration $\tau (< 1.5 \mu\text{s})$, while traps are switched off to avoid trap potentials.

The dynamics of this system is governed by the many-body Hamiltonian:

$$\hat{H} = \frac{\hbar\Omega}{2} \sum_i \hat{\sigma}_x^{(i)} - \frac{\hbar\delta}{2} \sum_i \hat{\sigma}_z^{(i)} + \sum_{i \neq j} V_{i,j} \hat{n}_r^{(i)} \hat{n}_r^{(j)}, \quad (1)$$

where the first term describes the coherent laser coupling between $|g_i\rangle$ and $|r_i\rangle$ of atom i with the transition operator $\hat{\sigma}_x^{(i)} = |g_i\rangle \langle r_i| + |r_i\rangle \langle g_i|$. The second term is the energy offset induced by the two-photon detuning δ from the ground-Rydberg transition. We focus on resonant excitation $\delta = 0$ in this work. The third term represents coherent interactions between two Rydberg atoms, where $\hat{n}_r^{(i)} = |r_i\rangle \langle r_i|$ is the Rydberg population operator acting on atom i and $V_{i,j}$ is the van der Waals interaction between atoms i and j .

After applying the excitation lasers, we switch on the traps again, where only atoms in $|g\rangle$ are recaptured, while atoms in $|r\rangle$ escape from the traps due to the antitrapping potential. Therefore, the time-evolved wave function is projected onto the $\{|g\rangle, |r\rangle\}$ basis. After turning the magnetic field off, we record the final atomic configuration via fluorescence imaging. We note that the interaction between nD -Rydberg states have anisotropic character $V_{i,j} = C_6(\theta_{i,j})/R_{i,j}^6$ [27], where $R_{i,j}$ is the atomic separation and $C_6(\theta_{i,j})$ is the interaction coefficient depending on the angle $\theta_{i,j}$ between the interaction axis and quantization axis \hat{z} . Therefore, the blockade radius defined by $|C_6(\theta)|/R_b^6 = \hbar\Omega$ also is anisotropic.

III. NUMERICAL SIMULATION MODEL

The experimental system described in the previous section has various physical limitations and technical imperfections which result in discrepancies from the pure Hamiltonian given by Eq. (1). To predict the dynamics in the presence of these imperfections, we modify the pure Hamiltonian. The physical

limitations and technical imperfections can be divided into the following three types. One arises from a single-atom level and leads to damping or dephasing of Rabi oscillations between ground and Rydberg states. As studied in [23], (i) off-resonant scattering from an intermediate state, (ii) spontaneous emission from a Rydberg state, (iii) Doppler shift due to atomic temperature, and (iv) laser phase noise belong to this type. In addition, (v) shot-to-shot fluctuation of detuning and (vi) shot-to-shot fluctuation of Rabi frequencies also lead to damping of the Rabi oscillations. The second type comes from a single-atom level but does not contribute to damping of Rabi oscillations, i.e., (vii) state detection error for ground and Rydberg states. We extend a model of detection errors investigated in [23] to N atom systems. The third type is multiparticle effects which lead to damping of many-body dynamics. We consider (viii) inhomogeneous Rabi frequencies and (ix) fluctuations of interactions caused by atomic position disorders.

Our model is based on a Lindblad master equation and a Monte Carlo method. A single-shot time evolution of an N -atom system is computed by the Lindblad master equation:

$$\dot{\hat{\rho}} = -\frac{i}{\hbar}[\hat{H}, \hat{\rho}] + \hat{\mathcal{L}}[\hat{\rho}], \quad (2)$$

where \hat{H} represents the system Hamiltonian given by Eq. (1), $\hat{\rho}$ is a $2^N \times 2^N$ density matrix, and $\hat{\mathcal{L}}$ is a sum of three Lindblad superoperators:

$$\hat{\mathcal{L}}_m[\hat{\rho}] = \sum_i \left(\hat{L}_m^{(i)} \hat{\rho} \hat{L}_m^{(i)\dagger} - \frac{1}{2} \{ \hat{L}_m^{(i)\dagger} \hat{L}_m^{(i)}, \hat{\rho} \} \right), \quad (3)$$

$$\hat{\mathcal{L}}_r[\hat{\rho}] = \sum_i \left(\hat{L}_r^{(i)} \hat{\rho} \hat{L}_r^{(i)\dagger} - \frac{1}{2} \{ \hat{L}_r^{(i)\dagger} \hat{L}_r^{(i)}, \hat{\rho} \} \right), \quad (4)$$

$$\hat{\mathcal{L}}_l[\hat{\rho}] = \hat{L}_l \hat{\rho} \hat{L}_l^\dagger - \frac{1}{2} \{ \hat{L}_l^\dagger \hat{L}_l, \hat{\rho} \}, \quad (5)$$

where \hat{L}_m and \hat{L}_r describe spontaneous emission from $|m\rangle$ and $|r\rangle$, respectively. \hat{L}_l represents a global dephasing due to laser phase noise. The Monte Carlo method is used to simulate shot-to-shot fluctuations of detuning, Rabi frequencies, atomic positions, and atomic velocities. In the following, we describe the numerical model for all nine effects.

(i) $|g\rangle$ and $|r\rangle$ are off-resonantly coupled to the intermediate state $|m\rangle = |5P_{3/2}, F=3, m_F=3\rangle$ by the 780- and 480-nm lasers, respectively. The total scattering rate estimated from the single-photon Rabi frequencies and the intermediate detuning is typically $\gamma_m/(2\pi) \approx 30$ kHz. For simplicity, the Lindblad operator in Eq. (3) is modeled by $\hat{L}_m^{(i)} = \sqrt{\gamma_m/2} \hat{\sigma}_z^{(i)}$.

(ii) The lifetime of the Rydberg state is simply modeled by the Lindblad operator: $\hat{L}_r^{(i)} = \sqrt{\Gamma_r} |g_i\rangle \langle r_i|$, where an effective lifetime composed of blackbody and radiative decay is used to estimate the decay rate Γ_r . For $55D_{5/2}$ ($63D_{5/2}$) Rydberg states, $\Gamma_r/(2\pi)$ is ≈ 11.5 kHz (≈ 8.2 kHz).

(iii) The atomic temperature leads to Doppler shift, which leads to dephasing. At atomic temperature $T = 35$ μ K, the width of the Doppler shift distribution is ≈ 46 kHz in a counterpropagating beam configuration of our excitation lasers. To model this effect, we modify the Rabi frequency $\Omega_i(\tau) = \Omega_0 e^{i\mathbf{k} \cdot \mathbf{R}_i(\tau)}$, where $\mathbf{R}_i(\tau) = \mathbf{R}_i + \delta \mathbf{R}_i + \mathbf{v}_i \tau$ is the time-dependent position of atom i , $\mathbf{k} = \mathbf{k}_{780} + \mathbf{k}_{480}$ is an

effective wave vector of the excitation lasers, \mathbf{R}_i is the fixed trap position of atom i , and $\delta \mathbf{R}_i$ and \mathbf{v}_i are randomly generated three-dimensional position and velocity vector, respectively. As each trap approximately has a harmonic potential, the position-velocity distribution of the trapped atom follows a Maxwell-Boltzmann law; that is, the standard deviations of the position of the atom in axial and radial directions of the trapping laser are $\approx (0.14, 0.75)$ μ m, and the standard deviation of the velocity of the atom is ≈ 58 nm/ μ s.

(iv) The excitation lasers have phase noise composed of different frequencies, which results in dephasing of Rabi oscillations [23,24,28]. Due to the difficulties in quantifying the laser phase noise, we use a global dephasing model described in Eq. (5), where the Lindblad operator $\hat{L}_l = \sum_i \sqrt{\gamma_l/2} \hat{\sigma}_z^{(i)}$ describes effective dephasing. To estimate γ_l , chi-square values are calculated for independently measured single-atom Rabi oscillations, while other parameters are fixed. The optimal value of $\gamma_l/(2\pi)$ is typically ≈ 0.22 MHz comparable to a sum of linewidths of frequency-locking error signals for the 780- and 480-nm lasers.

(v) Since the ground-Rydberg transition used in this work is sensitive to the external magnetic field with 2.8 MHz/G sensitivity, fluctuation of the magnetic field effectively results in shot-to-shot detuning fluctuation that is estimated as ≈ 28 kHz in our current system. In addition, fluctuations of the excitation laser frequencies of ≈ 50 kHz and light shift fluctuation of ≈ 49 kHz caused by the intensity variance of the excitation lasers are taken into account. The total fluctuation is $\sigma_\delta/(2\pi) \approx 127$ kHz.

(vi) The fluctuation of the driving Rabi frequency is induced by the intensity fluctuation of the excitation lasers. The fluctuation estimated from measured intensity noise is $\sigma_{\Omega_0} \approx 0.05\Omega_0$. The shot-to-shot fluctuations of the Rabi frequency Ω_0 and the detuning δ are assumed to follow the normal distribution functions with the standard deviations σ_{Ω_0} and σ_δ , respectively.

(vii) Regarding detection errors in state measurements, since an atom loss is interpreted as $|r\rangle$ in our detection scheme, losing atoms in $|g\rangle$ during the sequence leads to the detection error $\epsilon = P(r|g)$ in the measurement of $|r\rangle$. The atom loss is mainly caused by background gas collisions and nonunity recapture efficiency. The experimental value of ϵ is obtained from $\epsilon = 1 - P_0(0)^{1/N}$, where $P_0(0)$ is the probability of having zero Rydberg atoms at $\tau = 0$. The measured value of ϵ is typically 0.01–0.03. In addition, we have a finite error $\epsilon' = P(r|g)$ to detect Rydberg atoms. The error ϵ' is mainly caused by the spontaneous emission from $|r\rangle$ to $|g\rangle$ before the atom escapes from the trapping region. This process leads to wrongly inferring the excited atoms as being in $|g\rangle$. Our numerical simulation including the effective lifetime τ_{eff} of Rydberg state $55D_{5/2}$ ($63D_{5/2}$) and measured atomic temperature gives $\epsilon' \approx 0.05$ (≈ 0.03), which is approximately consistent with a recent investigation [23]. These detection errors alter actual probabilities $\tilde{P}_{ijk\dots}$ of detecting the $|ijk\dots\rangle$ state. For example, one of the state probabilities including the detection errors (ϵ, ϵ') for $N = 2$ atoms is given by

$$P_{gg} = (1 - \epsilon)^2 \tilde{P}_{gg} + (1 - \epsilon)\epsilon' \tilde{P}_{gr} + \epsilon'(1 - \epsilon) \tilde{P}_{rg} + \epsilon'^2 \tilde{P}_{rr}. \quad (6)$$

Similarly, P_{gr} , P_{rg} , and P_{rr} are composed of $2^2 = 4$ state probabilities \tilde{P}_{ij} .

(viii) Due to the limited power of the 480-nm laser, the laser is focused down to $w_{480} \approx 13 \mu\text{m}$ ($\approx 6 \mu\text{m}$) for $55D_{5/2}$ ($63D_{5/2}$) state experiments, while the beam waist of the 780-nm laser is $w_{780} \approx 45 \mu\text{m}$ for both experiments. While the excitation lasers are carefully aligned to maximize light shifts and an ionization loss rate of an atom trapped at the center of the system [29], the reduction of the Rabi frequency is found when atoms are prepared at a distance from the center. The spatial dependence of the Rabi frequency is numerically studied in [30], where a calibration factor relative to the values at the center of the beam is used to obtain the position-dependent Rabi frequency. Our model includes the position-dependent Rabi frequency as $\Omega_i(\tau)\alpha(\mathbf{R}_i)$, where $\Omega_i(\tau)$ and \mathbf{R}_i are the time-dependent Rabi frequency and the trap position of atom i , respectively. $\alpha(\mathbf{r}) = \alpha_{780}(\mathbf{r})\alpha_{480}(\mathbf{r})$ are laser field amplitudes relative to their values at the center of the beam:

$$\alpha_m(\mathbf{r}) = \frac{1}{\sqrt{1 + (z/z_{R_m})^2}} e^{-(x^2+y^2)/w_m^2(z)}, \quad (7)$$

where $z_{R_m} = \pi w_m^2/\lambda_m$ is the Rayleigh length, w_m is the beam waist, $w_m(z) = w_m\sqrt{1 + z^2/z_{R_m}^2}$ is the position-dependent beam waist, and the index $m = 780, 480$ represents the 780- and 480-nm excitation lasers, respectively.

(ix) Since interactions between Rydberg states are sensitive to the interatom separation, fluctuations of the separation and velocities of the atoms change the interaction strength [31,32]. Thus, we modify the interaction $V_{i,j}(\tau) = C_6/|\mathbf{R}_i(\tau) - \mathbf{R}_j(\tau)|^6$, where $\mathbf{R}_i(\tau)$ is the time-dependent position of atom i explained in effect (iii).

IV. EXPERIMENTAL RESULTS

We experimentally measure many-body dynamics in two different interaction regimes. For regime I, all pairwise interactions $|V_{ij}|$ are larger than the driving Rabi frequency $\hbar\Omega$. By varying the system size under a constant nearest-neighbor separation of atoms, we observe Rydberg blockade as well as blockade breaking. For regime II, only nearest neighbors have strong interactions. In this case, dynamics evolve under no simultaneous excitations of adjacent atoms.

For regime I, $|V_{i,j}| > \hbar\Omega$ for all i and j , we use small arrays containing up to $N = 4$ atoms with the nearest-neighbor spacing of $d \approx 3.0 \mu\text{m}$. The atomic geometries are shown in Fig. 2 (left panels). The arrays are resonantly driven to Rydberg state $|r\rangle = |63D_{5/2}, m_J = 5/2\rangle$. For the $N = 2$ case [Fig. 2(b)] where the atoms are aligned along the $\theta = 0^\circ$ axis, the interaction strength is estimated as $|V(d, 0^\circ)| \approx 2\pi\hbar \times 77.8 \text{ MHz}$. Since the single-atom Rabi frequency $\Omega \approx 2\pi \times 1.15 \text{ MHz}$ is much smaller than the interaction strength, we expect the system to be in the fully blocked regime. The observed Rydberg fraction f_r shows oscillations with a frequency of $(1.43 \pm 0.02)\Omega$, compatible with the expected frequency $\sqrt{2}\Omega$. For the equilateral triangle configuration with $N = 3$ atoms [Fig. 2(c)], the pairwise interactions depend on the angle θ due to the anisotropic characters of the $nD_{5/2}$ Rydberg states. The interaction strength for atom pairs aligned along the $\theta = 60^\circ, 120^\circ$ axis is weaker

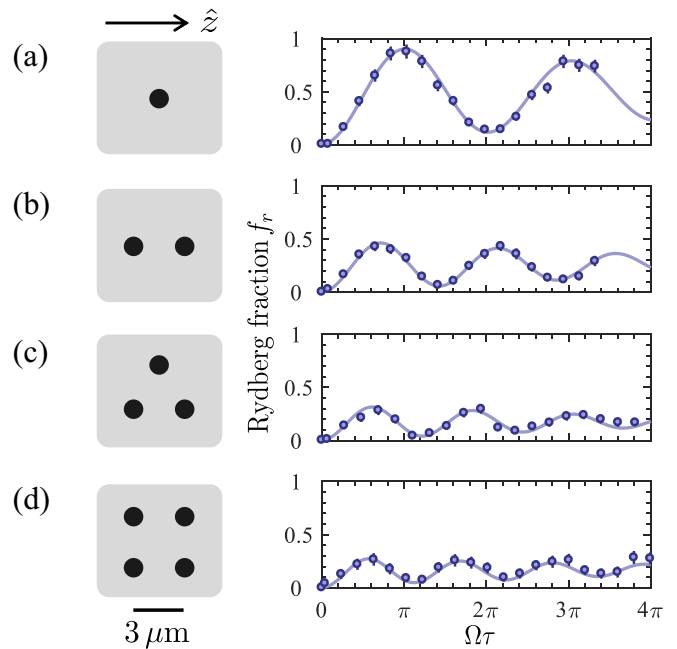


FIG. 2. Collective Rabi oscillations for various atom numbers $N = 1-4$. Each left panel shows the atomic configuration with lattice spacing of $d \approx 3.0 \mu\text{m}$: (a) one atom located in the system center, (b) $N = 2$ atoms aligned along the quantization axis \hat{z} , (c) a triangular configuration of $N = 3$ atoms, and (d) a $N = 4$ square array. The horizontal axis in the right panels is calibrated by independently measured single-atom Rabi frequency. Each point represents the experimental data, and the error bars show the standard error of the mean. The solid lines are the numerical simulation of the dynamics.

than that along $\theta = 0^\circ$. The reduction ratio of the interaction strengths is estimated as $|V(d, 60^\circ)|/|V(d, 0^\circ)| = |V(d, 120^\circ)|/|V(d, 0^\circ)| \approx 0.37$. Despite the interaction reduction, the measured f_r still indicates the blocked character, that is, the oscillation frequency of $(1.71 \pm 0.08)\Omega$, where $\Omega \approx 2\pi \times 1.49 \text{ MHz}$.

For the 2×2 square array [Fig. 2(d)], although any atom pair distances are smaller than the blockade radius including the angular dependence, the measured oscillation frequency $(1.89 \pm 0.04)\Omega$ is clearly lower than the fully blocked condition $\sqrt{4}\Omega$. This is mainly caused by blockade breaking due to finite blockade strength. The interaction strength between $\theta = 90^\circ$ pairs is $|V(d, 90^\circ)|/|V(d, 0^\circ)| \approx 0.39$, comparable to $\theta = 60^\circ, 120^\circ$ pairs in the triangle geometry. However, diagonal pairs in the 2×2 square array have a separation of $\sqrt{2}d \approx 4.24 \mu\text{m}$, which is close to the blockade radius $R_b(45^\circ) \approx 5.0 \mu\text{m}$ obtained from $|V(R_b, 45^\circ)| = \hbar\Omega$, where $\Omega \approx 2\pi \times 1.65 \text{ MHz}$ is the single-atom Rabi frequency. The results of the numerical simulation are shown in the solid lines of Fig. 2; the details of the model are presented in Sec. III. Our experimental results in the strong interaction regime and the blockade-breaking regime are consistent with the numerical simulations for the observed timescale $4\pi/\Omega \sim 1.5 \mu\text{s}$.

In the results discussed so far, the atoms are aligned within a blocked volume. For systems larger than the blockade volume, the initial state is coupled to multiple excited states with various coupling strengths. For regime II, we use two different geometries: a linear array of $N = 5$ atoms and a ring

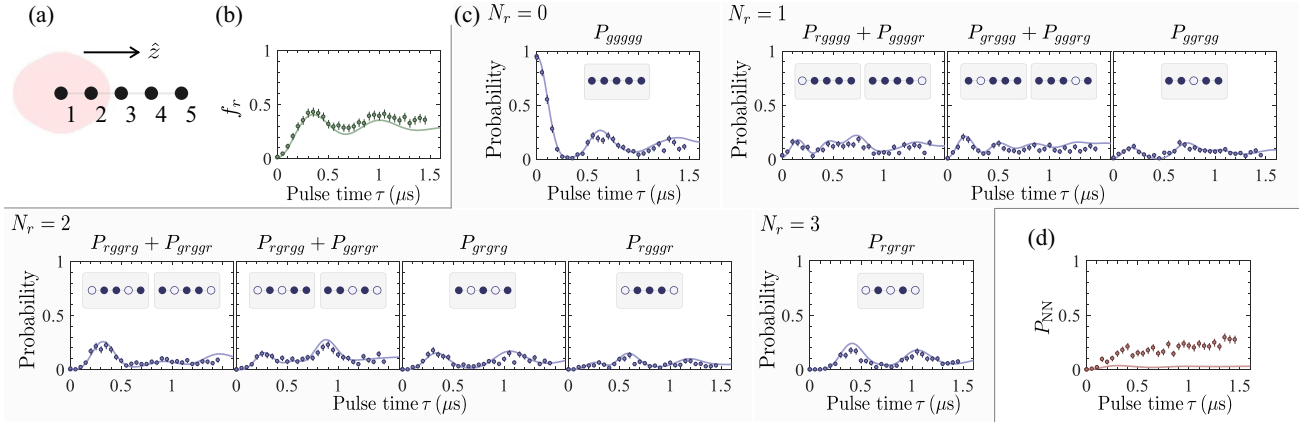


FIG. 3. Experimental data and numerical simulation results for a linear array with $N = 5$ atoms coupled to $|r\rangle = |55D_{5/2}, m_J = 5/2\rangle$. (a) Atomic geometries and estimated blockade volume (shaded area). (b) Evolution of the Rydberg fraction f_r . (c) Many-body state probabilities for each symmetric state where there are no adjacent Rydberg excitations. Each gray panel shows the corresponding many-body state, where solid circles represent the ground state $|g\rangle$ and open circles are the Rydberg states $|r\rangle$. (d) Probability of having nearest-neighbor excitations P_{NN} . Each point corresponds to about 140 repetitions of the experiment. The solid lines are the results of the numerical simulation.

array of $N = 6$ atoms. For both configurations, the nearest-neighbor interaction strength is larger, and the next-nearest one is smaller than the single-atom Rabi frequency, i.e., $|V_{i,i+1}| > \hbar\Omega > |V_{i,i+2}|$. In this case, simultaneous excitations of adjacent atoms are almost suppressed, while the next-nearest-neighbor interactions are approximately neglected. The system dynamics evolve under a restricted Hilbert space where there are no neighboring Rydberg excitations.

The $N = 5$ linear array is aligned along the $\theta = 0^\circ$ axis with a spacing of $d \approx 3.0 \mu\text{m}$, as shown in Fig. 3(a). Each atom is initialized in $|g\rangle$ and then coherently coupled to $|r\rangle = |55D_{5/2}, m_J = 5/2\rangle$ with a Rabi frequency of $\Omega \approx 2\pi \times 1.02 \text{ MHz}$, which results in a nearest-neighbor interaction of $|V_{i,i+1}| \approx 2\pi\hbar \times 18.9 \text{ MHz} > \hbar\Omega$, while a next-nearest-neighbor interaction is $|V_{i,i+2}| \approx 2\pi\hbar \times 0.3 \text{ MHz} < \hbar\Omega$. The shaded regime in Fig. 3(a) illustrates the range of the blockade volume. The radius along the \hat{z} axis $R_b \approx 4.88 \mu\text{m}$ is smaller than the array length $4d$. The observed Rydberg fraction f_r displayed in Fig. 3(b) increases up to ~ 0.43 , and the oscillation amplitude quickly damps due to multiple coupling strengths. This behavior indicates multiple excitations in the system.

To probe the excitation dynamics operating in the nearest-neighbor interaction regime in detail, we analyze many-body-state probabilities. Assuming a fully nearest-neighbor blockade, there is a total of 18 many-body states $|ijk\dots\rangle$ ($i, j, k, \dots \in \{g, r\}$) in the constrained Hilbert space. The rest of the many-body states include neighboring Rydberg atoms. As symmetrical many-body states have similar dynamics due to the global excitation process, these 18 many-body states are divided into nine different symmetric bases. Figure 3(c) shows the probabilities to observe each symmetric configuration: a global ground state (P_{ggggg}), three singly excited states ($P_{\text{rgggg}} + P_{\text{gggrg}}$, $P_{\text{rgrgg}} + P_{\text{ggrrg}}$, P_{grrgg}), four doubly excited states ($P_{\text{rrggg}} + P_{\text{grggg}}$, $P_{\text{rgrgg}} + P_{\text{grrgr}}$, P_{grgrg} , P_{rgrgr}), and a triply excited state (P_{rgrgr}). Here, $P_{ijk\dots}$ stands for the probability to detect a many-body state $|ijk\dots\rangle$. The individual symmetric configurations have multiple oscillation frequencies depend-

ing on the number of states coupled via the excitation laser. The overall behavior, such as oscillation frequencies and peak positions, is in agreement with the numerical simulations (solid lines), while one observes small differences, especially at longer excitation times.

To see the nearest-neighbor blockade, we plot the probability of having nearest-neighbor excitations P_{NN} in Fig. 3(d). We find that the observed probability has higher values than that expected from the numerical model, and the difference increases with the excitation time τ . We attribute the discrepancies to the complex level structure of interacting Rydberg atoms. In our model, multilevel effects such as neighboring Rydberg states and their Zeeman structure are not taken into account.

Similarly, we measure excitation dynamics in a ring geometry with $N = 6$ atoms coupled to $|r\rangle = |55D_{5/2}, m_J = 5/2\rangle$ [Fig. 4(a)]. Due to the anisotropic interaction, the interaction strength between atom pairs $|V_{1,2}| = |V_{3,4}| = |V_{4,5}| = |V_{6,1}| \approx 2\pi\hbar \times 6.9 \text{ MHz}$ is weaker than $|V_{2,3}| = |V_{5,6}| \approx 2\pi\hbar \times 18.9 \text{ MHz}$ when the atoms are equally separated. The driving single-atom Rabi frequency is tuned to $\Omega \approx 2\pi \times 1.28 \text{ MHz}$, which is smaller than any nearest-neighbor interactions $|V_{i,i+1}|$ but larger than any next-nearest-neighbor interactions $|V_{i,i+2}|$. The resulting Rydberg fraction f_r , displayed in Fig. 4(b), initially rises up to ~ 0.38 and then oscillates with small amplitudes. The numerical simulation captures the initial rise, although the observed values of f_r slightly stay above for longer excitation times. The time evolution of the many-body-state probability for each symmetric basis is shown in Fig. 4(c). The overall oscillations are consistent with the numerical model, while the differences clearly exist at longer times. These discrepancies result from unexpected neighboring excitations, as shown in Fig. 4(d). The observed nearest-neighbor excitation probability P_{NN} increases with increasing time, which we attribute again to multilevel effects.

V. DISCUSSION

In the previous section, the experimentally observed many-body dynamics in various atomic geometries and interaction

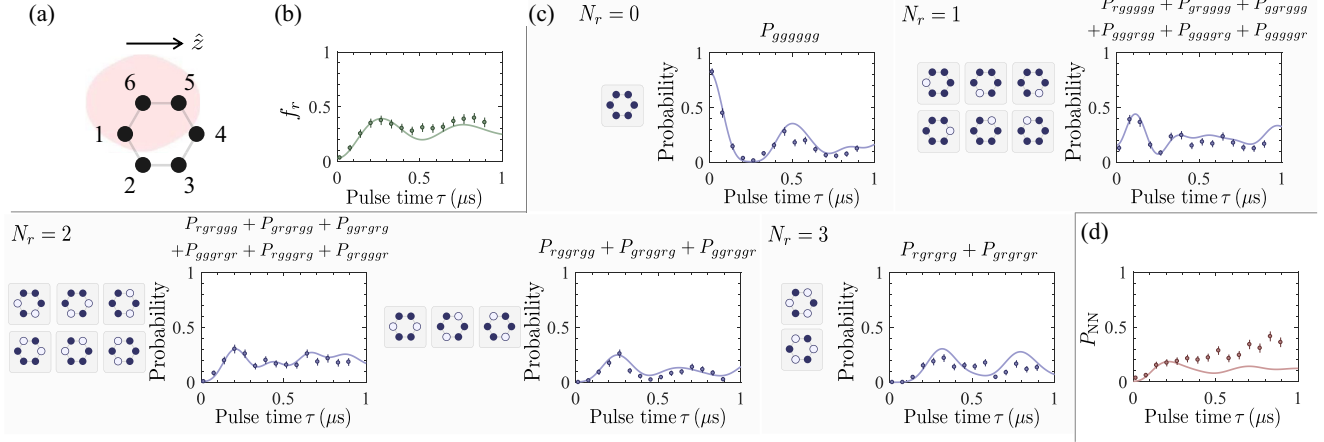


FIG. 4. Experimental data and numerical simulation results for a ring array with $N = 6$ atoms coupled to $|r\rangle = |55D_{5/2}, m_J = 5/2\rangle$. (a) Atomic geometries and estimated blockade volume (shaded area) which exhibits anisotropy. (b) Evolution of the Rydberg fraction f_r . (c) Many-body state probabilities for each symmetric state where there are no adjacent Rydberg excitations. A total of five symmetric configurations is represented with respect to the number of excitations. Each gray panel shows the corresponding many-body state, where solid circles represent the ground state $|g\rangle$ and open circles are the Rydberg states $|r\rangle$. (d) Probability of having nearest-neighbor excitations P_{NN} . Each point corresponds to about 120 repetitions of the experiment. The solid lines are the results of the numerical simulation.

ranges is compared with the numerical model described in Sec. III. In this section, we discuss the comparison between the numerical simulation and observed data.

For regime I, $|V_{i,j}| > \hbar\Omega$ for all i and j , the experimental data are consistent with the numerical simulations (Fig. 2), which allows us to quantify contributions of individual imperfections. For example, in Fig. 5(a) Rydberg fractions in the $N = 2$ array obtained from the numerical model with each imperfection (solid lines) are compared with that from the pure Hamiltonian (dotted lines), where the shaded area indicates differences. The comparison shows that our current system is mainly limited by technical imperfections, which are phase noise of excitation lasers [effect (iv)] and shot-to-

shot fluctuation of Rabi frequencies [effect (vi)]. The other effects are small for the observed time range but they are accumulated and can affect the dynamics. In particular, damping of Rabi oscillations due to finite laser phase noise is a consistent result with recent experiments [23,28].

For the 2×2 array [Fig. 5(b)], we find that not only effects (iv) and (vi) but also effect (ix), fluctuation of Rydberg interaction strengths, lead to the visible discrepancies. This is because diagonal pairs in the 2×2 array are close to the region $V \sim \hbar\Omega$, in which the dynamics includes several frequencies depending on the interaction strength [33]. The fluctuation of the interaction strength thus leads to dephasing in the dynamics of many-body states. Our simulation indicates

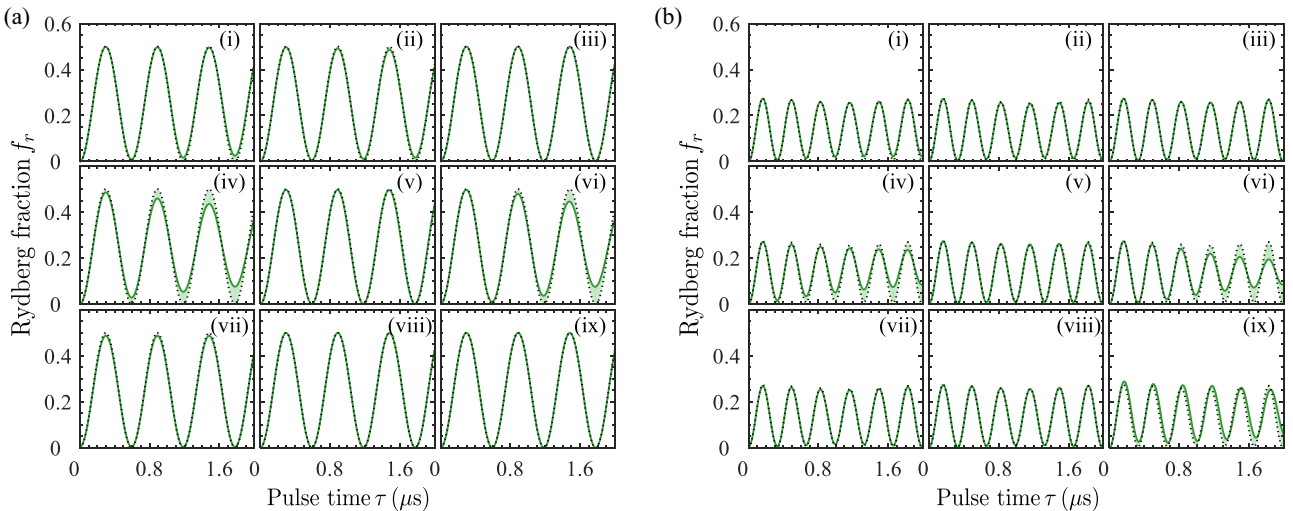


FIG. 5. The effects of the individual error sources for experimental conditions used in (a) an $N = 2$ linear array and (b) an $N = 4$ square array. The Rydberg fraction f_r , including each error source (solid lines) is compared with the ideal situation obtained from the pure Hamiltonian (dotted lines). As the error sources, we take into account (i) off-resonant scattering from the intermediate state, (ii) spontaneous emission from the Rydberg state, (iii) the Doppler effect, (iv) laser phase noise, (v) the fluctuation of detuning, (vi) the fluctuation of the Rabi frequency, (vii) finite detection errors, (viii) the inhomogeneous Rabi frequency, and (ix) the fluctuation of Rydberg-Rydberg interaction strengths.

that the effect of interaction fluctuation decreases again when atoms are in the nearest-neighbor interaction regime.

For regime II, $|V_{i,i+1}| > \hbar\Omega > |V_{i,i+2}|$, we show differences between the numerical simulation and experimental data. In particular, the observed probabilities of nearest-neighbor excitations increase with excitation time [Figs. 3(d) and 4(d)]. This behavior indicates that the blockade condition is broken even for the nearest-neighbor excitation being suppressed for our experimental parameters ($|V_{i,i+1}| > \hbar\Omega$). They are attributed to the complex level structure of interacting Rydberg atoms that are not taken into account for our model. By the dipole-dipole Hamiltonian, pairs of atoms in $|r\rangle$ are weakly coupled to other Rydberg states (e.g., other Zeeman sublevels), which are dark to the excitation laser. Thus, the population of excited states is gradually increased. Such a violation of the blockade condition was observed in $nD_{3/2}$ Rydberg state experiments [18], and the dependence on external fields (magnetic and electric) was recently studied in [34]. However, it is challenging to numerically simulate many-body dynamics including all relevant Rydberg states even for a small number of atoms.

There are several prospects from technical and physical perspectives to improve the fidelity of the quantum simulations. (i) Off-resonant scattering from the intermediate state can be decreased by using different two-photon excitation schemes and by increasing excitation laser intensities and detunings from the intermediate state. Instead of them, a direct single-photon transition is an alternative approach. Sideband cooling of atoms strongly confined in microtraps [35,36] would be an essential technique to reduce the Doppler effect [effect (iii)] as well as the fluctuation of Rydberg-Rydberg interaction strengths [effect (ix)]. Effect (iv), laser phase noise, can be significantly decreased by resonator filtering as demonstrated in [28], and the sample-hold stabilization

technique helps to suppress drifts of fast pulse intensities [effect (vi)]. Effect (vii), state detection errors, can be reduced by field ionization of Rydberg atoms or by projecting Rydberg states onto different ground states. In addition, finding optimal parameters for mapping the multilevel structure of interacting Rydberg atoms onto ideal models [34] is an important step. Furthermore, the number of atoms in this work is limited by nondeterministic loading and can be increased by implementing atom-by-atom rearrangements [10–15], efficient loading methods [37–39], or their combination.

VI. CONCLUSION

We have demonstrated many-body dynamics in various interaction regimes, where up to six atoms are confined in one- and two-dimensional arrays and coupled to $nD_{5/2}$ -Rydberg states. The experimentally observed results have been analyzed with a numerical model which includes various physical limitations and technical imperfections arising not only from the single-atom level [23] but also from the multiparticle level. By modeling these error sources, we have identified the effects of individual errors on the observed dynamics, which provide useful information towards an improvement in the abilities of experimental simulations. These processes are an essential step for scaling up the number of atoms.

ACKNOWLEDGMENTS

This work was supported by the Japan Society for the Promotion of Science (Grants No. 17H02935 and No. 17J07843) and was partly supported by a research grant from the Matsuo Academic Foundation. T.Y. acknowledges support from the Research and Educational Consortium for Innovation of Advanced Integrated Science (CIAiS).

-
- [1] I. M. Georgescu, S. Ashhab, and F. Nori, Quantum simulation, *Rev. Mod. Phys.* **86**, 153 (2014).
 - [2] T. D. Ladd, F. Jelezko, R. Laflamme, Y. Nakamura, C. Monroe, and J. L. O'Brien, Quantum computers, *Nature (London)* **464**, 45 (2010).
 - [3] H.-J. Briegel, T. Calarco, D. Jaksch, J. I. Cirac, and P. Zoller, Quantum computing with neutral atoms, *J. Mod. Opt.* **47**, 415 (2000).
 - [4] M. Saffman, Quantum computing with atomic qubits and Rydberg interactions: Progress and challenges, *J. Phys. B* **49**, 202001 (2016).
 - [5] C. Gross and I. Bloch, Quantum simulations with ultracold atoms in optical lattices, *Science* **357**, 995 (2017).
 - [6] T. Xia, M. Lichtman, K. Maller, A. W. Carr, M. J. Piotrowicz, L. Isenhower, and M. Saffman, Randomized Benchmarking of Single-Qubit Gates in a 2D Array of Neutral-Atom Qubits, *Phys. Rev. Lett.* **114**, 100503 (2015).
 - [7] Y. Wang, A. Kumar, T. Y. Wu, and D. S. Weiss, Single-qubit gates based on targeted phase shifts in a 3D neutral atom array, *Science* **352**, 1562 (2016).
 - [8] F. Nogrette, H. Labuhn, S. Ravets, D. Barredo, L. Béguin, A. Vernier, T. Lahaye, and A. Browaeys, Single-Atom Trapping in Holographic 2D Arrays of Microtraps with Arbitrary Geometries, *Phys. Rev. X* **4**, 021034 (2014).
 - [9] H. Tamura, T. Unakami, J. He, Y. Miyamoto, and K. Nakagawa, Highly uniform holographic microtrap arrays for single atom trapping using a feedback optimization of in-trap fluorescence measurements, *Opt. Express* **24**, 8132 (2016).
 - [10] D. Barredo, S. de Léséleuc, V. Lienhard, T. Lahaye, and A. Browaeys, An atom-by-atom assembler of defect-free arbitrary two-dimensional atomic arrays, *Science* **354**, 1021 (2016).
 - [11] M. Endres, H. Bernien, A. Keesling, H. Levine, E. R. Anschuetz, A. Krajenbrink, C. Senko, V. Vuletic, M. Greiner, and M. D. Lukin, Atom-by-atom assembly of defect-free one-dimensional cold atom arrays, *Science* **354**, 1024 (2016).
 - [12] W. Lee, H. Kim, and J. Ahn, Three-dimensional rearrangement of single atoms using actively controlled optical microtraps, *Opt. Express* **24**, 9816 (2016).
 - [13] H. Kim, W. Lee, H. Lee, H. Jo, Y. Song, and J. Ahn, In situ single-atom array synthesis using dynamic holographic optical tweezers, *Nat. Commun.* **7**, 13317 (2016).
 - [14] D. Barredo, V. Lienhard, S. de Léséleuc, T. Lahaye, and A. Browaeys, Synthetic three-dimensional atomic structures assembled atom by atom, *Nature (London)* **561**, 79 (2018).

- [15] A. Kumar, T.-Y. Wu, F. Giraldo, and D. S. Weiss, Sorting ultracold atoms in a three-dimensional optical lattice in a realization of Maxwell's demon, *Nature (London)* **561**, 83 (2018).
- [16] M. Saffman, T. G. Walker, and K. Mølmer, Quantum information with Rydberg atoms, *Rev. Mod. Phys.* **82**, 2313 (2010).
- [17] A. Browaeys and T. Lahaye, Many-body physics with individually controlled Rydberg atoms, *Nat. Phys.* **16**, 132 (2020).
- [18] H. Labuhn, D. Barredo, S. Ravets, S. de Léséleuc, T. Macrì, T. Lahaye, and A. Browaeys, Tunable two-dimensional arrays of single Rydberg atoms for realizing quantum Ising models, *Nature (London)* **534**, 667 (2016).
- [19] H. Bernien, S. Schwartz, A. Keesling, H. Levine, A. Omran, H. Pichler, S. Choi, A. S. Zibrov, M. Endres, M. Greiner, V. Vuletić, and M. D. Lukin, Probing many-body dynamics on a 51-atom quantum simulator, *Nature (London)* **551**, 579 (2017).
- [20] H. Kim, Y. J. Park, K. Kim, H.-S. Sim, and J. Ahn, Detailed Balance of Thermalization Dynamics in Rydberg-Atom Quantum Simulators, *Phys. Rev. Lett.* **120**, 180502 (2018).
- [21] V. Lienhard, S. de Léséleuc, D. Barredo, T. Lahaye, A. Browaeys, M. Schuler, L.-P. Henry, and A. M. Läuchli, Observing the Space- and Time-Dependent Growth of Correlations in Dynamically Tuned Synthetic Ising Models with Antiferromagnetic Interactions, *Phys. Rev. X* **8**, 021070 (2018).
- [22] D. Barredo, H. Labuhn, S. Ravets, T. Lahaye, A. Browaeys, and C. S. Adams, Coherent Excitation Transfer in a Spin Chain of Three Rydberg Atoms, *Phys. Rev. Lett.* **114**, 113002 (2015).
- [23] S. de Léséleuc, D. Barredo, V. Lienhard, A. Browaeys, and T. Lahaye, Analysis of imperfections in the coherent optical excitation of single atoms to Rydberg states, *Phys. Rev. A* **97**, 053803 (2018).
- [24] W. Lee, M. Kim, H. Jo, Y. Song, and J. Ahn, Coherent and dissipative dynamics of entangled few-body systems of Rydberg atoms, *Phys. Rev. A* **99**, 043404 (2019).
- [25] N. Schlosser, G. Reymond, and P. Grangier, Collisional Blockade in Microscopic Optical Dipole Traps, *Phys. Rev. Lett.* **89**, 023005 (2002).
- [26] C. Tuchendler, A. M. Lance, A. Browaeys, Y. R. P. Sortais, and P. Grangier, Energy distribution and cooling of a single atom in an optical tweezer, *Phys. Rev. A* **78**, 033425 (2008).
- [27] N. Šibalić, J. D. Pritchard, C. S. Adams, and K. J. Weatherill, ARC: An open-source library for calculating properties of alkali Rydberg atoms, *Comput. Phys. Commun.* **220**, 319 (2017).
- [28] H. Levine, A. Keesling, A. Omran, H. Bernien, S. Schwartz, A. S. Zibrov, M. Endres, M. Greiner, V. Vuletić, and M. D. Lukin, High-Fidelity Control and Entanglement of Rydberg-Atom Qubits, *Phys. Rev. Lett.* **121**, 123603 (2018).
- [29] Y. Miroshnychenko, A. Gaëtan, C. Evellin, P. Grangier, D. Comparat, P. Pillet, T. Wilk, and A. Browaeys, Coherent excitation of a single atom to a Rydberg state, *Phys. Rev. A* **82**, 013405 (2010).
- [30] K. Gillen-Christandl, G. D. Gillen, M. Piotrowicz, and M. Saffman, Comparison of Gaussian and super Gaussian laser beams for addressing atomic qubits, *Appl. Phys. B* **122**, 131 (2016).
- [31] M. Marcuzzi, J. Minář, D. Barredo, S. de Léséleuc, H. Labuhn, T. Lahaye, A. Browaeys, E. Levi, and I. Lesanovsky, Facilitation Dynamics and Localization Phenomena in Rydberg Lattice Gases with Position Disorder, *Phys. Rev. Lett.* **118**, 063606 (2017).
- [32] M. Ostmann, J. Minář, M. Marcuzzi, E. Levi, and I. Lesanovsky, Non-adiabatic quantum state preparation and quantum state transport in chains of Rydberg atoms, *New J. Phys.* **19**, 123015 (2017).
- [33] L. Béguin, A. Vernier, R. Chicireanu, T. Lahaye, and A. Browaeys, Direct Measurement of the van der Waals Interaction between Two Rydberg Atoms, *Phys. Rev. Lett.* **110**, 263201 (2013).
- [34] S. de Léséleuc, S. Weber, V. Lienhard, D. Barredo, H. P. Büchler, T. Lahaye, and A. Browaeys, Accurate Mapping of Multilevel Rydberg Atoms on Interacting Spin-1/2 Particles for the Quantum Simulation of Ising Models, *Phys. Rev. Lett.* **120**, 113602 (2018).
- [35] A. M. Kaufman, B. J. Lester, and C. A. Regal, Cooling a Single Atom in an Optical Tweezer to Its Quantum Ground State, *Phys. Rev. X* **2**, 041014 (2012).
- [36] J. D. Thompson, T. G. Tiecke, A. S. Zibrov, V. Vuletić, and M. D. Lukin, Coherence and Raman Sideband Cooling of a Single Atom in an Optical Tweezer, *Phys. Rev. Lett.* **110**, 133001 (2013).
- [37] T. Grünzweig, A. Hilliard, M. McGovern, and M. F. Andersen, Near-deterministic preparation of a single atom in an optical microtrap, *Nat. Phys.* **6**, 951 (2010).
- [38] B. J. Lester, N. Luick, A. M. Kaufman, C. M. Reynolds, and C. A. Regal, Rapid Production of Uniformly Filled Arrays of Neutral Atoms, *Phys. Rev. Lett.* **115**, 073003 (2015).
- [39] M. O. Brown, T. Thiele, C. Kiehl, T.-W. Hsu, and C. A. Regal, Gray-Molasses Optical-Tweezer Loading: Controlling Collisions for Scaling Atom-Array Assembly, *Phys. Rev. X* **9**, 011057 (2019).